Cerebral Cortex, March 2018;28: 949–962

doi: 10.1093/cercor/bhw420
Advance Access Publication Date: 3 February 2017
Original Article

ORIGINAL ARTICLE

Multimodal MRI Imaging of Apoptosis-Triggered Microstructural Alterations in the Postnatal Cerebral Cortex

Volodymyr Petrenko[1], Yohan van de Looij[2,3,‡], Jevgenia Mihhailova[1], Patrick Salmon[1], Petra S. Hüppi[2], Stéphane V. Sizonenko[2,†] and Jozsef Z. Kiss[1,†]

[1]Department of Neurosciences, University of Geneva Medical School, Geneva, Switzerland, [2]Division of Child Growth & Development, Department of Pediatrics, University of Geneva, Geneva, Switzerland and [3]Laboratory for Functional and Metabolic Imaging, Ecole Polytechnique Fédérale de Lausanne, Lausanne, Switzerland

Address correspondence to Prof. Jozsef Zoltan Kiss, Department of Fundamental Neurosciences, University of Geneva Medical School, Rue Michel-Servet 1, CH-1211 Geneva 4, Switzerland. Email: Jozsef.Kiss@unige.ch

[†]S. V. Sizonenko and J. Z. Kiss contributed equally to this work as senior authors.

[‡]V. Petrenko and Y. van de Looij contributed equally to this work.

Abstract

Prematurely born children often develop neurodevelopmental delay that has been correlated with reduced growth and microstructural alterations in the cerebral cortex. Much research has focused on apoptotic neuronal cell death as a key neuropathological features following preterm brain injuries. How scattered apoptotic death of neurons may contribute to microstructural alterations remains unknown. The present study investigated in a rat model the effects of targeted neuronal apoptosis on cortical microstructure using in vivo MRI imaging combined with neuronal reconstruction and histological analysis. We describe that mild, targeted death of layer IV neurons in the developing rat cortex induces MRI-defined metabolic and microstructural alterations including increased cortical fractional anisotropy. Delayed architectural modifications in cortical gray matter and myelin abnormalities in the subcortical white matter such as hypomyelination and microglia activation follow the acute phase of neuronal death and axonal degeneration. These results establish the link between mild cortical apoptosis and MRI-defined microstructure changes that are reminiscent to those previously observed in preterm babies.

Key words: apoptosis, brain development, cortical plasticity, magnetic resonance imaging, white matter injury

Introduction

Prematurity is the most important cause of cognitive, behavioral, and socialization deficits in childhood (Johnson and Marlow 2011). The rate of preterm birth ranges from 7% to 11% of all live births worldwide (Beck et al. 2010) and up to 50% of these infants may exhibit subsequent neurological and behavioral disabilities (Volpe 2009). The neuropathology of the human premature brain remains elusive. It has been proposed that the underlying pathology termed "encephalopathy of prematurity" is the result of a combined effect of an initial destruction and the subsequent delay in gray matter development, especially in the cerebral cortex (Volpe 2009). The causal relationship between destructive processes and delayed growth impairment remains obscure. Emerging evidence indicates that even in the absence of any overt

damage in the brain, preterm survivals exhibit reduced gray matter volume accompanied by cognitive disorders (Inder et al. 2005; Dubois et al. 2008; Ball et al. 2012). Diffusion tensor magnetic resonance imaging (MRI) in human infants and newborn lambs revealed that reduced gray matter volume is paralleled by MRI-defined microstructural changes consisting of a delayed reduction of fractional anisotropy (FA) that is normally occurring during postnatal development (Ball et al. 2013; Dean et al. 2013; Vinall et al. 2013). A recent ex vivo study of the brain of fetal lambs that has experienced intrauterine ischemia suggests that microstructure alterations could be correlated with a delayed maturation of dendritic arbors (Dean et al. 2013). In addition, human neuropathological studies show that white matter injuries in perinatal period result in delayed neuronal loss in the different regions of developing brain (Pierson et al. 2007; Andiman et al. 2010; Northington et al. 2011; Kinney et al. 2012). While it has been speculated that perinatally occurring scattered apoptotic cell death in the cortical gray matter may contribute to the encephalopathy of prematurity (Johnston et al. 2001; Wasterlain et al. 2002; Folkerth 2005; Zhu et al. 2005), the impact of such lesion on subsequent development of the cerebral cortex remains unknown. In particular, the effects of apoptotic lesion on MRI-defined microstructural maturation have not been explored. This is related, at least partially to the difficulties to detect and monitor subtle and diffuse apoptotic death with MRI techniques due to the variability in onset and location of apoptotic lesions.

Therefore, in approaching this issue, we took advantage of a well-established rat model of targeted neuronal ablation utilizing a diphtheria toxin (DT) and diphtheria toxin receptor (DTR) systems (Petrenko et al. 2015). The model allows the precise spatiotemporal control of moderate apoptotic neuronal death in the cerebral cortex. To examine microstructural changes, we used a multimodal approach of MRI and proton magnetic resonance spectroscopy (^{1}H-MRS) techniques combined with neuronal reconstruction and histological analysis. We hypothesized that scattered neuronal apoptosis in the developing cortex could induce acute and long-term microstructural changes that are reminiscent to those observed in encephalopathy of prematurity.

Materials and Methods

Animals

All described experiments were conducted in accordance with the Swiss laws and were previously approved by the Geneva Cantonal Veterinary Authority. Wistar rats were provided by Charles River Laboratories.

Plasmids

For introducing a high affinity receptor to diphtheria toxin (DTR), the plasmid pCLX-UBI-DTR_IRES-tRFP was used as an experimental construct. This plasmid expresses DTR together with the turbo red fluorescent protein (tRFP) (Evrogen) for labeling and tracking of electroporated cells. The plasmid pCLX-UBI-GFP encoding green fluorescent protein (GFP) was used as a control. Details on these plasmids and the procedures that have been used for their preparation can be obtained at (http://lentilab.unige.ch/). For principal experiments, the plasmid mix included 2.4 μg/μL of experimental plasmid and 2.6 μg/μL of control plasmid was electroporated in order to control electroporation pattern.

In Utero Electroporation and DTR Cell Death Induction

In utero electroporation was performed on the embryonic day 16 (E16), allowing continuation of gestation in utero. The procedure was done as described previously (Saito and Nakatsuji 2001). About 1 μL of DNA solution (5 μg/μL of plasmid diluted in 10 M Tris-HCl, PH 8.0 and mixed with Fast green colorant, 1:1000, Sigma-Aldrich) was injected unilaterally through the uterine wall into the lateral ventricle of the fetus using mouth-controlled aspirator tube for calibrated microcapillary pipette (Sigma-Aldrich) under the control of colorant distribution in the ventricle. Electric field was generated by square waved electroporator (NepaGene, CUY21SC) and exposed between platinum forceps electrodes (d = 0.5 cm, NepaGene, CUY611P3-1) in the way to label part of fetal subventricular zone which gives origin for neurons in somatosensory cortex (positive electrode was posed on injected hemisphere, axis between 2 electrodes made angle 45–60° with sagittal axis of the head). The following settings of electroporator were used: voltage 50 V, exposure time 50 msec, time between pulses 950 msec, number of pulses 5.

Death of DTR electroporated cells was induced by single subcutaneous injection DT at P15 in dose 50 μg/kg. Due to the slight excess of the control plasmid, single control cells survived in the apoptotic neighborhood.

Tissue Processing and Immunohistochemistry

Under the pentobarbital anesthesia animals were perfused intracardially with 0.9% saline followed by 4% paraformaldehyde (PFA). Then brains were postfixed in 4% PFA overnight. Of the note, 50 μm coronal sections were obtained with Leica vibratome then incubated for 1 h in blocking solution (phosphate buffered saline (PBS), 0.5% bovine serum albumin and 0.3% Triton X-100) and with the primary antibodies diluted in the same solution overnight at 4 °C. After rinsing 3 times in PBS, slices were incubated with complementary secondary antibodies, diluted in PBS with 0.5% bovine serum albumin for 1.5 h. Hoechst (Invitrogen, Molecular probes) staining was performed at final step of the procedure to visualize the nuclei. The following primary antibodies have been used: Mouse anti-CD68 (1:100, AbD Serotec), rabbit anti-GFAP (glial fibrillary acidic protein) (1:2500, Dako Cytomation), mouse anti-GFAP (1:2500, Millipore), goat anti-GFP (1:2500, Novus Biologicals), mouse anti-glutamine synthetase (GS) (1:200, Millipore), rabbit anti-Iba1 (1:2500, Wako), mouse anti-NeuN (1:500, Millipore), rabbit anti-tRFP (1:1000, Evrogen). To recognize the signal, following secondary antibodies were used: anti-rabbit Alexa-488, Alexa-568, Alexa-647; anti-mouse Alexa-488, Alexa-568, and Alexa-647; anti-goat Alexa-488, Alexa-568, and Alexa-647 (1:1000, Molecular Probes by Invitrogen). TUNEL assay (Roche) and Fluoro-Jade B (Millipore) staining were done according to the manufacture protocols.

Reconstruction of Dendritic Tree

Dendritic tree of the neurons labeled by electroporation was reconstructed using a computer-based Neurolucida system (MicroBrightField) on 60 μm thick coronal sections with ×40 objective on a Nikon microscope (Nikon Corporation). Only stellate cells in layer IV recognized by the small size of the cell body and absence of the apical dendrite were chosen for reconstructions. A morphometric analysis of total dendritic length and dendritic complexity including numbers of primary dendrites and secondary branch points (nodes) was performed with Neurolucida Explorer software (MicroBrightField). Distribution of the dendritic arbors from the cell body was expressed on the polar histograms where 0 degree corresponds to the apical part of the cell facing the cortical surface. At least 25 control cells and

dying cells from 4 animals were reconstructed for each P15 control group and at 3 and 5 days after DT injection. At least 45 surviving labeled cells were reconstructed from 5 animals at 14 days after DT injection and in age-matched control.

Electron Microscopy

For electron microscopy studies, brains were perfused with 2% PFA containing 2.5% of glutaraldehyde in 0.1 M PBS. Of the note, 300 μm coronal vibratome slices were obtained with Leica vibratome and postfixed in the fixative solution for 1 h at 4 °C. The regions from external capsule were dissected under binocular microscope. After postfixation in OsO_4, further rinsing and dehydration through ascending series of ethanol concentrations and absolute acetone (3 changes for 5 min), the samples were infiltrated through graded acetone/Epon mixtures (1:1, 1:3, 2 h each) and immersed overnight in Epon resin. Flat embedding in Epon was used. Ultrathin sections (40–50 nm thick) were cut on an LKB 8800 ultratome (Sweden), stained with uranyl acetate and lead citrate, and examined with a Tecnai Electron Microscope (FEI) at 80 Kv.

In Vivo ^{1}H-MR Spectroscopy and Diffusion Tensor Imaging Studies

MR experiments were performed 3 days (n = 11), 5 days (n = 11), and 14 days (n = 8) post DT injection (DPI) on an actively-shielded 9.4 T/31 cm magnet (Varian/Magnex) equipped with 12-cm gradient coils (400 mT/m, 120 μs) using a quadrature transceive 17-mm surface RF coil. During measurements, rat was lying prone, its head secured via ear bars and continuously anesthetized under a flow of 1.5–2% isoflurane in oxygen. Body temperature was maintained at 37 ± 0.5 °C using thermoregulated water circulation. T_2-Weighted (T_2W) Fast Spin Echo images with time repetition (TR)/ time echo (TE) = 6000/80 ms; FOV = 25 × 25 mm and matrix size = 256 × 128 were realized to position MRS voxel of interest. First and second order shims were adjusted using FASTMAP (Gruetter and Tkac 2000). The water linewidths ranged between 8 and 12 Hz for voxel of interest of 1.5 × 1.5 × 3 mm^3. First a water spectrum was acquired as reference for quantification (8 averages) then spectra acquisitions within the cortical lesion and the contralateral cortical area of rats were performed using an ultra-short echo time (TE/TR = 2.7/4000 ms) SPECIAL spectroscopy method (Mlynarik et al. 2006). Twenty-two series of FIDs (16 averages each) were acquired.

Before DTI experiments, first and second order shims were adjusted using FASTMAP (Gruetter and Tkac 2000) resulting in a water linewidths of 16–20 Hz for a voxel of 5 × 7 × 7 mm^3 centered in the brain. For diffusion tensor imaging, a semi-adiabatic double spin echo sequence was used (van de Looij et al. 2011b) and diffusion gradients were positioned around the first 180° with the same polarity resulting in a b-value fixed to 1000 $s.mm^{-2}$ (δ/Δ = 3/23 ms and G = 26.6 G/cm) and applied along 21 spatial directions (Icosahedral 21 directions diffusion gradient sampling scheme [Hasan et al. 2001]). DT-EPI parameters were: FOV = 23 × 15 mm^2, matrix size = 128 × 64 zero-filled to 256 × 168, 8 slices of 0.8 mm thickness in the axial plane, 8 averages with TE/TR = 42/2000 ms.

^{1}H-MRS Analysis

Acquired spectra were individually corrected for frequency drift, summed together and corrected for residual eddy current effects using the reference water signal. Proton spectra were analyzed with LCModel (Provencher 1993) using the unsuppressed water signal corrected for age-dependent changes in brain water content as an internal reference (Tkac et al. 2003). Metabolites were quantified resulting in a neurochemical profile of the ipsilateral and the contralateral cortical area for each group. A Wilcoxon nonparametric paired test was used to compare statistically values between ipsilateral and contralateral ROIs, significance was reached when $P < 0.05$. For MRS results, a Bonferroni correction was applied on P values to correct for multiple measurements.

DTI Data Analysis

The extent of apoptotic region was delineated by the position of GFP-labeled cells on histological sections and regions of interest (ROIs) were manually delineated in the known apoptotic areas as well as in the contralateral position in the cortex and the external capsule. Diffusivity values (mean diffusivity – MD, parallel diffusivity – $D_{//}$, and orthogonal diffusivity – $D_{\perp}$) as well as FA was derived from the tensor by using a homemade Matlab (Mathworks) software and averaged in these ROIs. A Wilcoxon nonparametric paired test was used to compare statistically values between ipsilateral and contralateral ROIs, significance was reached when $P < 0.05$.

Immunostaining: Image Acquisition and Data Analysis

For post hoc analysis, immunostained sections were examined with a Nikon Eclipse 80i microscope using Nikon objectives and photographed with a digital camera (Retiga EX; Qimaging) under the control of Openlab software (version 3.1.2; Improvision). Confocal analysis was done with LSM 700 confocal microscope using Plan-Neofluar ×40 or ×60 Oil objectives (Zeiss). Image processing was performed with the program LSM Image Browser version 4.2.0.121 (Zeiss).

For quantification of labeled cells, confocal images from the sections at the level of barrel cortex were used. Electroporated region was recognized by the presence of fluorescent neurons. Except when indicated, images were taken from 3 adjacent areas within the somatosensory cortex from at least 3 coronal sections of at least 4 animals from a minimum of 2 independent experiments. Quantification of fluorescent cells was done using ImageJ software (version 1.45, ImageJ Inc.). Levels of astrogliosis and microglial reaction were quantified as surface density of GFAP and Iba1 fluorescence using Metamorph outline software (Molecular device).

The fiber density was quantified on confocal photos taken with ×60 oil objective from the region of external capsule aside from the cingulum. Images were taken from 3 coronal slices of 4 animals from at least 2 independent experiments. Number of tRFP-positive fibers crossing the line (length 50.81 μm), drawn perpendicularly to the main axonal direction, was quantified. Microglial Iba1-positive and CD68-positive cells in the external capsule were quantified using LSM Image Browser software (version 4.2.0.121) on confocal photos from 2 adjacent regions starting aside from the cingulum from 3 coronal slices of 5 brains.

For electron microscopy studies, the quantification of the myelinated fibers was performed on the microphotos taken with the same magnification from 10 random regions in 2 of 3 obtained blocks of the dissected ipsilateral and contralateral external capsules from 3 animals. For measurements of fiber diameter, axonal diameter, and g-ratio, 7 randomly chosen fibers from each photo (70 fibers per animal, n = 3 animals) were analyzed with the Tecnai software (FEI Tecnai).

Except when indicated, results are expressed as mean ± standard error of the mean (SEM), n = number of analyzed brains. Statistical significance was measured by Student t-test (paired, 2-tailed) and defined at $^{*}P < 0.05$, $^{**}P < 0.01$, or $^{***}P < 0.001$. For repeated measurements, one-way ANOVA test was used when compared one factor. All statistical tests were realized with GraphPad Prism 5 Software.

Results

Neuronal Lesioning

In order to induce apoptotic death of layer IV neuronal populations in the developing somatosensory cortex, we performed in utero electroporation of E16 rat embryos with a mixture of tRFP–DTR encoding vector and a GFP-encoding control plasmid (Fig. 1A,B and Supplementary Fig. S1A,B). Our electroporated cell population mainly comprised small granular neurons in layer IV but we also observed scattered layer II/III pyramidal cells. Consistent with labeling of this latter population, we found tRFP–DTR positive fibers in the external capsule as well as in the corpus callosum. Cell death was initiated by a single subcutaneous injection of DT at P15. Confirming previous observations (Petrenko et al. 2015), DT injection induced apoptotic death of layer IV and layer II/III DTR expressing neurons without disruption of blood-brain barrier, necrosis, and death of glial cells (Supplementary Fig. S2A–C).

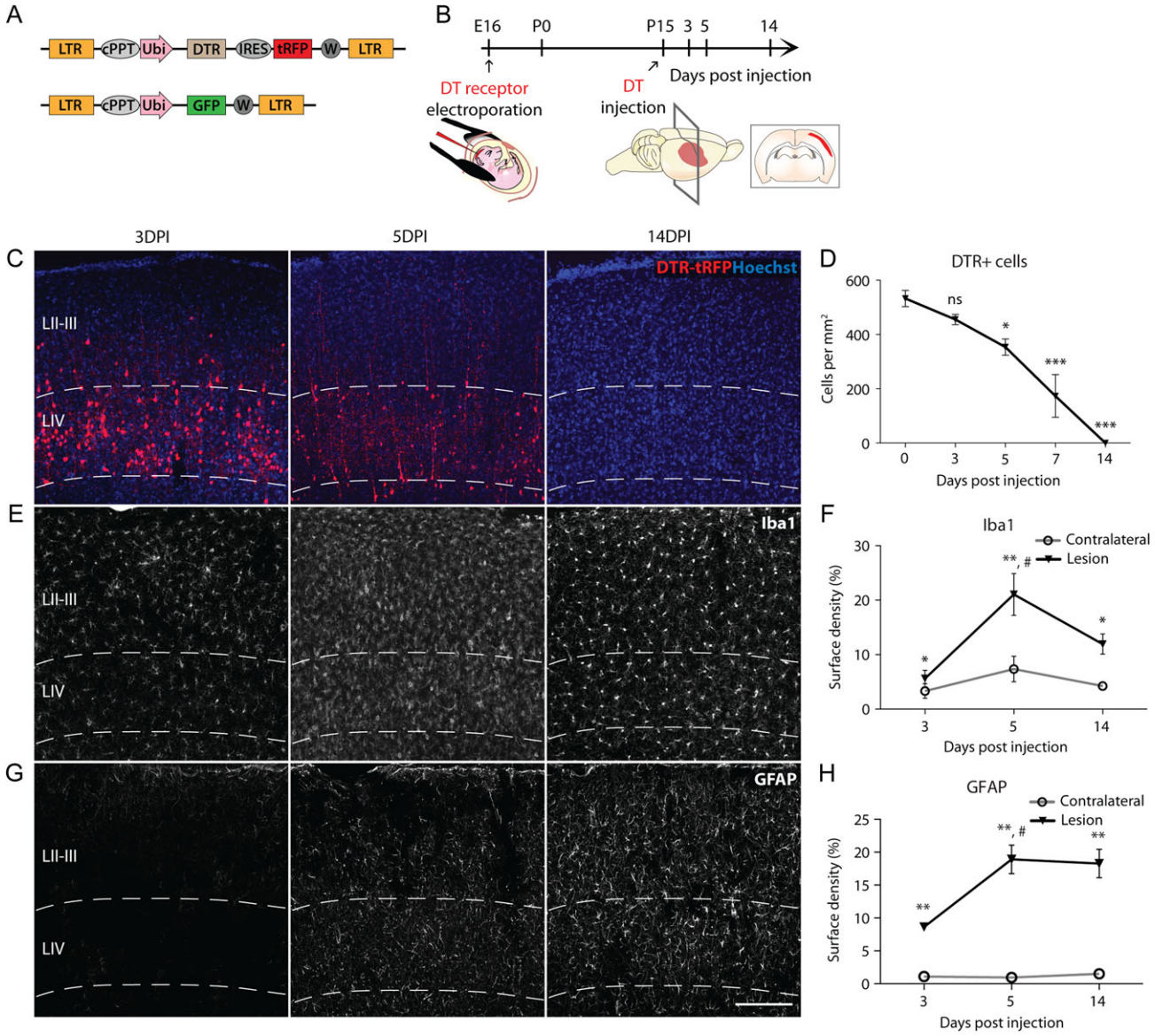

Figure 1. Histopathological changes following targeted ablation of neurons in the granular layer of the rat barrel cortex. (*A*) Schematic drawings of plasmid constructs that have been utilized in the study. (*B*) Timeline of the experimental procedures. (*C*) Representative confocal photos showing progressive death of DTR-positive neurons (labeled with tRFP) at the indicated time points and (*D*) Graph displaying loss of DTR-positive electroporated neurons during first 2 weeks after DT injection (data expressed as a mean ± SEM, $^{*}P < 0.05$, $^{***}P < 0.001$—statistically significant difference when compared with P15 control). (*E*) Confocal photos showing the distribution of microglial cells in the cortex immunostained for Iba1 at the indicated time points. (*F*) Graph representing surface area covered by Iba1-positive elements in granular layer of somatosensory cortex at the mentioned time points. (*G*) Reactive astrogliosis after neuronal death, which is displayed on the confocal photos of the cortex immunostained for GFAP and (*H*) Graph representing surface area covered by GFAP-positive elements. Data in *F* and *H* expressed as a mean ± SEM. $^{*}P < 0.05$, $^{**}P < 0.01$ (paired 2-tailed t-test for comparison between ipsilateral and contralateral cortices). $^{\#}P < 0.05$ (unpaired 2-tailed t-test when compared with the previous time point). Scale bar = 200 μm.

Progressive loss of tRFP–DTR neurons was observed starting from 3 days after DT injection. No tRFP–DTR-positive neurons in the layer were present 14 days after DT injection (14 DPI) (Fig. 1*C*,*D*). Quantitative analysis of surface density for Iba1-labeling (Fig. 1*E*) and GFAP (Fig. 1*G*) in granular layer confirmed the significant microglial reaction in the electroporated side starting already at 3 DPI and reaching highest level at 5 DPI correlating with slow neuronal death (Fig. 1*F*,*H*). In contrast to the decreasing microglial activity in the post-apoptotic cortex, the intensity of reactive astrogliosis remained high at 14 DPI. Notably, glial reactions were restricted to the apoptotic region (Supplementary Fig. S3).

^{1}H-MR Spectroscopy Detects Specific Changes of Neurochemical Compounds Following Neuronal Apoptosis

In order to search for clinically relevant correlates of programmed cell death of cortical neurons, we first carried out in vivo, noninvasive, ^{1}H-MRS. Good spectral quality was achieved, as judged from water line width ranging from 8 to 12 Hz (Fig. 2*A*). Due to the very thin cortical structure in the rat pup brain, MRS was performed on a small volume of 6.8 µL centered in granular layer of the cortex. On the overall study signal-to-noise ratio was equal in average to 24 ± 3. Such consistent data were subjected to spectral analysis and absolute quantification by LCModel provided the concentration of 17 metabolites.

Neuronal death was accompanied by a decline in the concentration of the neuronal markers: *N*-acetylaspartate (NAA) and *N*-acetylaspartylglutamate (NAAG) (Fig. 2*B*). Notably a drop in NAA concentration was present at 3 DPI in the beginning of the apoptotic period while decline in NAAG concentration was measured later at 5 DPI during the time of massive neuronal death (Fig. 2*B*; Supplementary Fig. S2*A*–*C*). Although, the level of these neuronal markers was still reduced at 14 DPI, the difference between lesion and contralateral hemispheres was not significant.

The concentration of glial marker myo-inositol (Ins) was increased in the cortex at 3 DPI and 5 DPI and rose further at 14 DPI (Fig. 2*C*); it was well correlated with the development of reactive astrogliosis.

The glutamate/glutamine ratio (Glu/Gln) in the post-apoptotic cortex was reduced at 5 DPI and 14 DPI (Fig. 2*D*) indicating a disturbance of Glu–Gln cycle between reactive astrocytes and glutamatergic neurons. This reduction resulted from an increase of Gln concentration at all time points but reached the level of significance only at 14 DPI. Notably, the concentration of Glu in the post-apoptotic tissue was not changed. Glutamine in the brain is synthesized from Glu and ammonia by the enzyme GS located in astrocytes. To evaluate whether the observed increase in Gln concentration in 14 DPI was associated with the overexpression of the appropriate enzyme by the reactive astroglia, we performed immunostaining for GS and quantified surface density of labeled elements. No significant difference in GS labeling between contralateral and lesion side was present (Supplementary Fig. S4*A*,*B*). Thus, elevated concentration of Gln seems to be independent of the level of the enzyme in astrocytes and may be related to its transportation or utilization by the glutamatergic neurons.

The concentration of the most stable brain metabolite, creatine (Cr) that is generally used for normalization of neurochemical compounds, was increased in the late post-apoptotic 14 DPI period (Fig. 2*E*). At the same time, the content of macromolecules was decreased in the post-apoptotic cortex.

Together these results demonstrate that "^{1}H-MR spectroscopy" can reveal metabolic perturbations that are specific for the acute or delayed phase of apoptotic neuronal death.

Apoptotic Neuronal Death is Associated with Alterations in Cortical Microstructure Defined by High-Field DTI

We next explored neuronal apoptosis-induced alterations in cortical macrostructure and microstructure. We failed to detect macrostructural alterations in the apoptotic region on anatomical T_2W images even in 5 DPI, the timing of high neuronal death (Fig. 3*A*,*B*). In order to gain information about microstructural changes, we used DTI to characterize water diffusion in sampled areas. Changes in axial and radial diffusivities ($D_{//}$ and $D_{\perp}$, respectively) were assessed on the FA maps derived from diffusion tensor experiments (Fig. 3*C*) with overlaid eigenvectors (Fig. 3*D*). In 5 DPI and 14 DPI, eigenvectors in the ipsilateral cortex had better alignment with increased space in between compared with contralateral one. The MD value was increased in the ipsilateral cortex at all experimental time points indicating important microstructural disturbances induced by neuronal apoptosis and subsequent cortical reorganization (Fig. 3*E*). In 3 DPI only $D_{//}$ but not $D_{\perp}$ was increased indicating an increase in water diffusion, thus reduced microstructure complexity toward the cortical surface. However, this disproportion between $D_{//}$ and $D_{\perp}$ values did not alter FA in the apoptotic cortex when compared with contralateral side. Starting from the 5 DPI, both $D_{//}$ and $D_{\perp}$ were proportionally increased without significant difference in FA values between ipsilateral and contralateral ROIs. These data demonstrate a proportional decrease in microstructural complexity during the apoptotic cell death process. In the post-apoptotic cortex at 14 DPI, all diffusivity values were still increased. However, at this time point FA was higher in the injured cortex than in the corresponding contralateral region indicating disproportional changes in water diffusivity in favor to the axial direction (Fig. 3*F*). Thus, noninvasive DTI techniques identify in vivo local microstructural abnormalities in the cortex following neuronal injury, displaying proportional decrease of microstructural complexity during the apoptotic period and disproportional changes in the post-apoptotic period.

Apoptotic Cell Death of Neurons Involves a Progressive Degeneration of Dendritic Arbors

Consistent with previous observations (Petrenko et al. 2015), our results above suggest that DT-induced cell death is a slowly progressing process (last for about 7 days) that is relevant to classical brain injury models. We hypothesized that dying neurons have an impact on the microstructural changes detected by DTI at 3 DPI and 5 DPI. We analyzed the complexity of the dendritic tree and the distribution of dendritic branches from the cell body of dying DTR-positive neurons, reconstructed utilizing Neurolucida software. At 3 DPI, dying neurons exhibited more simple morphology than control electroporated neurons at P15 without DT injection (Fig. 4*A*). The number of dendritic outgrowth as well as total length of dendritic tree in dying cortical neurons was progressively reduced after DT injection till 5 DPI (Fig. 4*B*). Notably, reduction of the dendritic tree was proportional in all directions from the perikaryon, which is visible on the polar histograms representing distribution of dendritic branches from the cell body (Fig. 4*C*). Thus, a slowly progressive

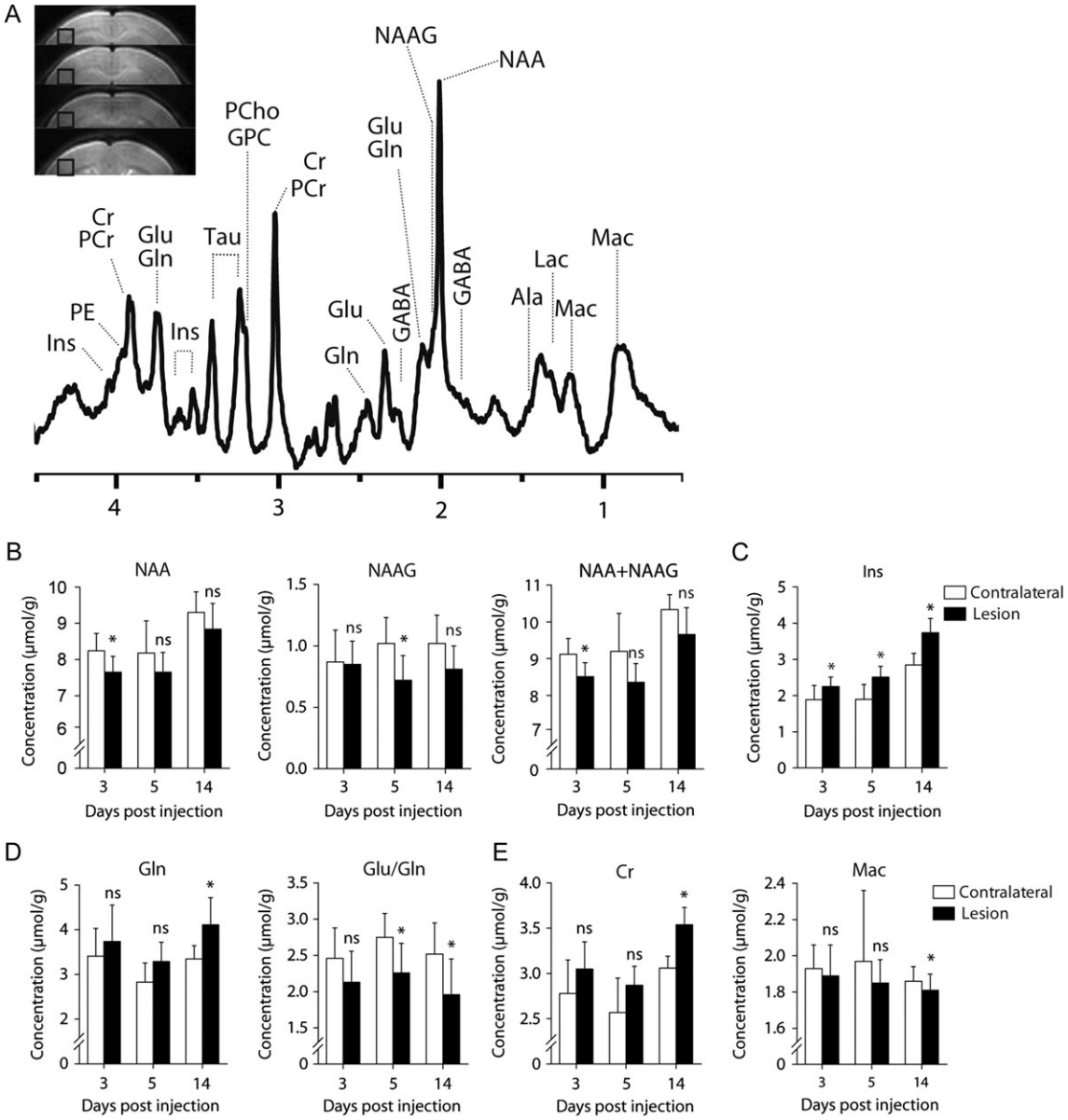

Figure 2. ^{1}H-MR spectroscopy showing specific changes of neurochemical compounds induced by neuronal ablation in the somatosensory cortex. (*A*) Typical spectrum in the lesioned cortex at 5 DPI at 9.4 T. Insert: Voxel of interest corresponding layer IV of somatosensory cortex displayed on a T_2W image. (*B–E*) Histograms representing concentration of metabolites showing significant differences between contralateral and ipsilateral cortices at the indicated time points (data expressed as a mean ± SD, *$P < 0.05$, Wilcoxon nonparametric paired test with Bonferoni correction). Mac, macromolecules; Asc, ascorbate; Ala, alanine; bhB, beta-hydroxybutyrate; PCho, phosphorylcholine; GPC, Glycerophosphocholine; Cr, creatine; PCr, phosphocreatine; GABA, γ-aminobutyric acid; Glc, glucose; Glu, glutamate; Gln, glutamine, Ins, myo-inositol; Lac, lactate; NAA, *N*-acetylaspartate; NAAG, *N*-acetylaspartylglutamate; PCr, phosphocreatine; PE, phosphoethanolamine; Tau, taurine.

decline in morphological complexity of dendritic arbors during apoptotic death is associated with a decrease of microstructural complexity identified by noninvasive DTI.

Increasing Dendritic Arbor Complexity of Neighboring Neurons in the Post-Apoptotic Cortex

In the post-apoptotic period, besides the reduction of neurons in the ipsilateral cortex, plastic changes may occur in adjacent surviving neurons. Utilizing an excess of the control GFP-coding plasmid in the electroporated mixture allowed the visualization and analysis of surviving neurons in the apoptotic neighborhood. GFP-positive cells were reconstructed utilizing Neurolucida software (Fig. 5A) and the dendritic arbors were analyzed as described above. The higher total dendritic length in injured cortex compared with control indicated an increase in the complexity of these cells in the apoptotic neighborhood (Fig. 5B). Interestingly, the reorganization of the dendritic tree was mainly occurring in radial direction as shown on the polar histograms (Fig. 5C). These findings indicate the presence of dendritic plasticity in the apoptotic injury neighborhood and their reorganization mainly in radial direction.

DTI Analysis Identifies Alterations in the Microstructure of White Matter

Focusing on the external capsule (Fig. 6A), the DTI analysis detected significant increase in $D_{//}$ but not in MD and $D_{\perp}$

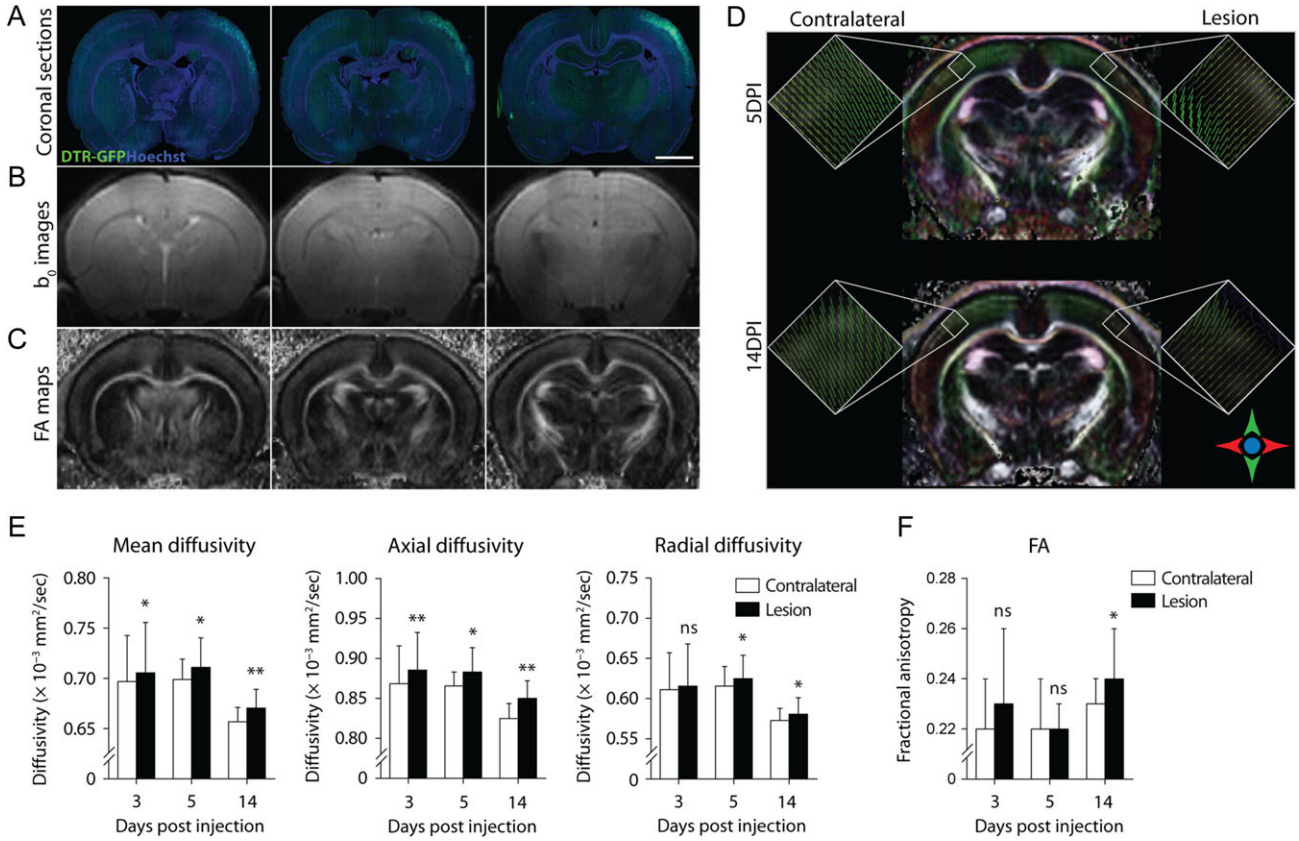

Figure 3. High-field DTI studies demonstrate local disturbances of cortical microstructure following neuronal death. (*A*) Coronal sections of the appropriate regions of the brain showing electroporation pattern marked by survived GFP-positive neurons (nuclei are stained with the Hoechst). These regions were used to delineate ROIs in the analysis of DTI. (*B*) Typical b_0 image and (*C*) FA maps obtained at 5 DPI. (*D*) Eigenvectors overlaid on a FA maps represent obvious changes in tissue organization between ipsilateral and contralateral hemispheres. White rectangles: Zoom in the regions of particular interest in the cortex. Color code indicates principal direction of eigenvectors. (*E*) Histograms displaying principal changes in the parameters of diffusivity (mean diffusivity (MD), axial ($D_{//}$), and orthogonal diffusivity ($D_{\perp}$)) in the injured and in the control, contralateral cortices at indicated time points. (*F*) Histogram showing increased degree of FA in the cortex following neuronal ablation. Data expressed as a mean ± SD, *P < 0.05, **P < 0.01 (Wilcoxon nonparametric paired test).

(Fig. 6*B*) neither in FA (Fig. 6*C*) at 3 DPI. At 5 DPI, diffusivity values (MD and $D_{\perp}$) were higher in the ipsilateral external capsule, indicating decreased microstructural complexity of the white matter (Fig. 6*B*). Remarkably, FA was lower in the ipsilateral external capsule than in the contralateral one, indicating asymmetrical changes in the diffusivity distribution. Finally, in 14 DPI at post-apoptotic period, a non-significant elevation of all the diffusivity values was present with a decrease of FA in the ipsilateral external capsule ($P = 0.055$, $n = 8$). These data demonstrate that noninvasive DTI analysis can detect specific microstructural changes in the subcortical white matter during the process of apoptotic death of cortical neurons.

Modified Water Diffusivity in the White Matter is Related to Delayed Histopathological Changes

Because we observed tRFP–DTR-positive fibers in the external capsule as well as in the corpus callosum, we hypothesized that axonal degeneration may underlie DTI-defined changes in the white matter. To test this, we first quantified the number of DTR-positive axons in the external capsule, which as expected was higher in the ipsilateral (665.9 ± 65.1 fibers/mm) then in the contralateral hemisphere (533.1 ± 68.5; $P = 0.0018$, 2-tailed paired *t*-test, $n = 4$). The density of DTR-positive fibers of the external capsule progressively decreased during the apoptotic period and they were completely absent in 2 weeks after DT injection (Fig. 7*A*,*B*).

To further characterize these changes, we performed electron microscopic analyses. As early as 3 DPI, we observed focal swelling of the axons with disruption and local disorganization of neurofilaments (Fig. 7*C*). Although the density of myelinated fibers on the tangential sections was not significantly different between ipsilateral and contralateral hemispheres, the mean diameter of the fibers was larger in the lesioned side because of axonal swelling as revealed by the increase of mean axonal diameter (Fig. 7*C*,*F*). In addition, we found an increase in *g*-ratio (axonal diameter to total fiber diameter) and thinning of the myelin thickness in the ipsilateral side indicating a reduced myelination of the fibers (Fig. 7*F*). The progression of axonal degeneration at 5 DPI was paralleled by the appearance of empty myelin sheath lacking axons (Fig. 7*D*). The percentage of such structures was 10.99 ± 1.98% in the ipsilateral external capsule compared with 1.83 ± 0.18% in contralateral side ($P = 0.017$, $n = 3$, 2-tailed, unpaired *t*-test). The density of myelinated fibers was 2 times less then in the contralateral external capsule (Fig. 7*D*,*F*). However, the diameter of the axons, myelin thickness and consequently, the fibers diameter and *g*-ratio values were not significantly different from the contralateral side. Important expansion of extracellular space was typical at this time point (Fig. 7*D*).

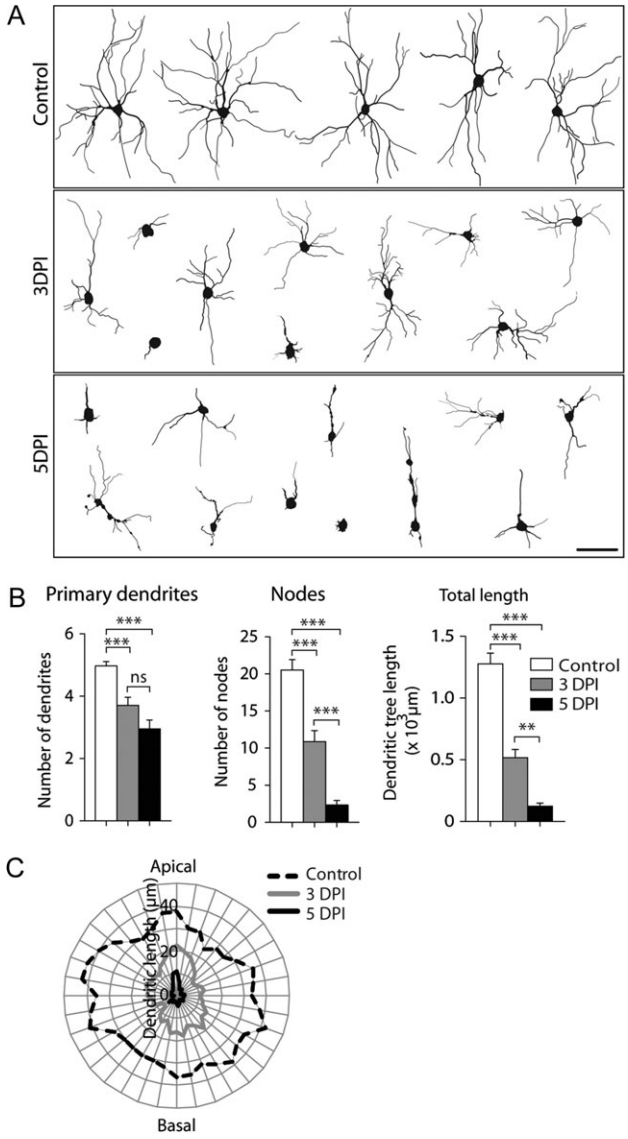

Figure 4. Decreased dendritic arbor complexity of dying neurons. (*A*) Neurolucida reconstructions of single electroporated neurons in layer IV under the control conditions and dying DTR-positive neurons at 3 DPI and 5 DPI. Scale bar = 50 µm. (*B*) Graphs displaying main characteristics of dendritic tree at indicated time points (number of primary dendrites, average number of branching points, and total length of dendrites). Data expressed as a mean ± SEM, $^{**}P < 0.01$ and $^{***}P < 0.001$ (unpaired 2-tailed *t*-test). (*C*) Polar histogram representing average distribution of the dendritic length based on the Neurolucida reconstruction where the polar axis represents the angle from cortical surface and *y*-axis represents the length of dendrites in micrometers (2-way ANOVA was used to test difference between groups, $P < 0.0001$ between matching angles).

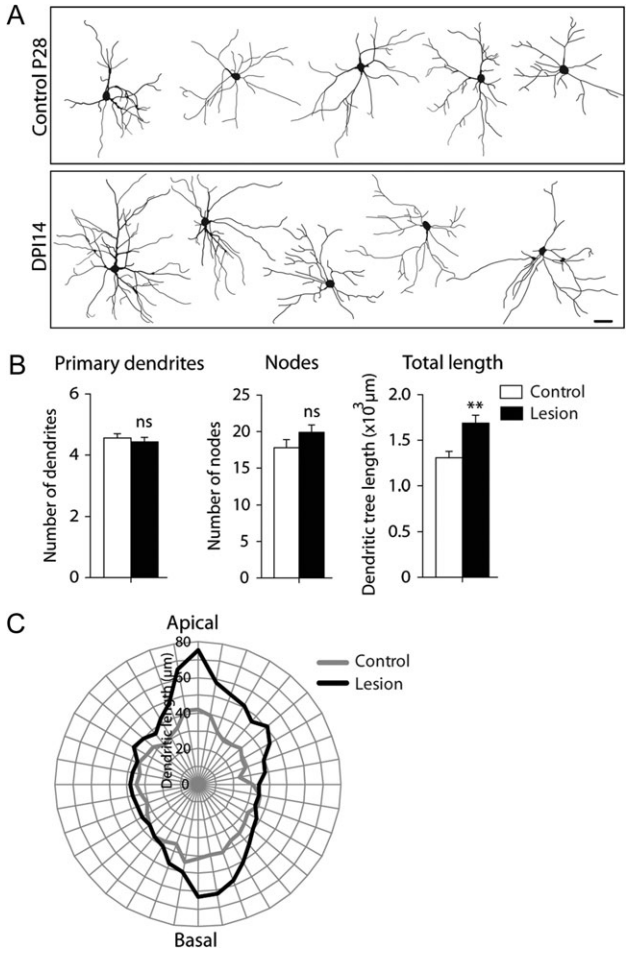

Figure 5. Increasing dendritic complexity of surviving neurons in the apoptotic neighborhood. (*A*) Neurolucida reconstructions displaying morphology of the electroporated neurons in layer IV under the control conditions and in the post-apoptotic region at 14 DPI. Scale bar = 50 µm. (*B*) Histograms displaying main dendritic characteristics indicating slight dendritic plasticity of neurons in the post-apoptotic area. Data expressed as a mean ± SEM, $^{**}P < 0.01$. (*C*) Polar histogram representing average distribution of the dendritic length based on the Neurolucida reconstruction where the polar axis represents the angle from cortical surface and the *y*-axis represents the length of dendrites in micrometers (2-way ANOVA was used to test difference between groups, $P < 0.0001$ between matching angles).

In order to assess the delayed effect of lesion in the external capsule, we also performed electron microscopy studies in 14 DPI when all DTR-positive axons have been eliminated. Comparing the density of myelinated fibers did not reveal significant difference between the ipsilateral and contralateral sides (Fig. 7*E*,*F*). Next, we measured the mean diameter of the fibers that was significantly higher in the ipsilateral external capsule than in the contralateral. The increase of fibers diameter was due to the significant increase of axonal diameter; however, the thickness of myelin sheath was almost 2 times less then in the contralateral side. Consequently the *g*-ratio value was higher in the lesioned side indicating hypomyelination of the fibers. Moreover, numerous fibers expressed signs of myelin degeneration such as intramyelinic edema and splitting of myelin sheath (Fig. 7*E*). It was still possible to observe degenerating fibers lacking axons that made up to 5.98 ± 1.87% in the ipsilateral external capsule and only 0.33 ± 0.17% in contralateral side ($P = 0.0399$, $n = 3$, 2-tailed unpaired *t*-test). Thus, apoptotic death of projection cortical neurons appears to induce first axonal dystrophy, mainly in the ipsilateral external capsule, followed by a degeneration of altered fibers and secondary myelin degeneration as well as hypomyelination of the neighboring fibers.

We then explored whether these ultrastructural changes were sufficient to recruit microglial cells. For this, a co-immunostaining for CD68, a marker of activated microglial cells, and Iba1, a marker of microglial cells, was applied (Fig. 8*A*). Although the number of microglial cells labeled with Iba1 was not significantly different in 3 DPI, the proportion of activated CD68-positive forms was 2 times

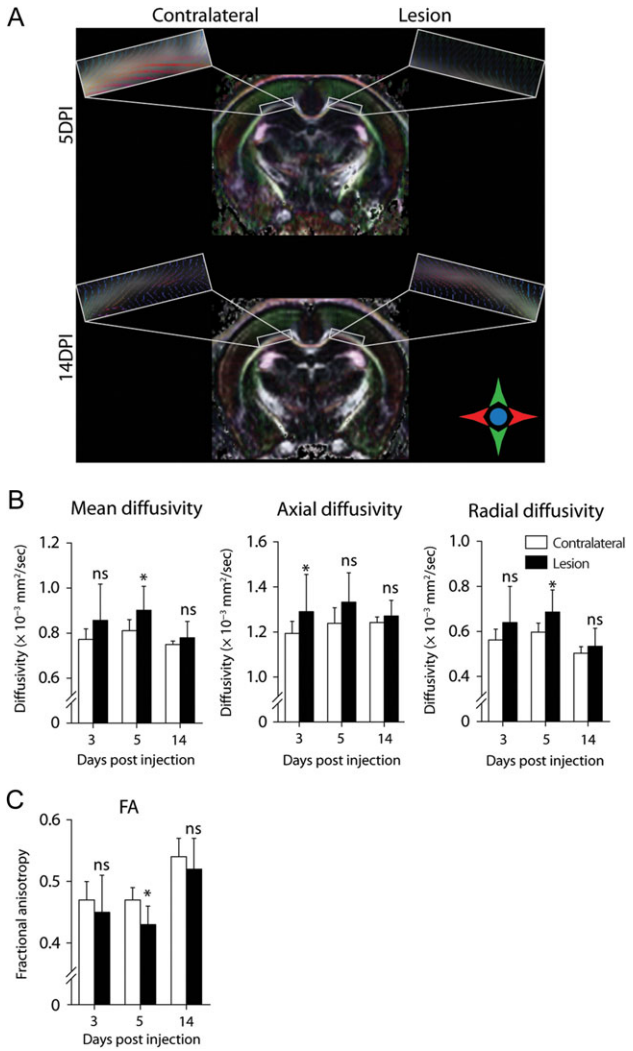

Figure 6. White matter changes: High-field DTI detects lesion in external capsule following neural ablation in the cortex. (*A*) Eigenvectors overlaid on a FA maps showing changes in tissue organization between ipsilateral and contralateral hemispheres with the focus on external capsule (zoomed in the white rectangles). Color code indicates principal direction of eigenvectors. (*B*) Graphs representing changes in the parameters of diffusivity (mean diffusivity (MD), axial ($D_{//}$), and orthogonal diffusivity ($D_{\perp}$)) in the external capsule at indicated time points. (*C*) FA in the external capsule following neuronal ablation in the cortex. Data expressed as a mean ± SD, $^{*}P < 0.05$ (Wilcoxon nonparametric paired test).

higher than in contralateral external capsule (Fig. 8*B*). Axonal degeneration at 5 DPI resulted in the significant increase in number of microglial cells with the prevalence of their activated subpopulation ipsilaterally (Fig. 8*A*,*B*; Supplementary Fig. S5). Notably, at 14 DPI, the number of Iba1-positive cells in the ipsilateral external capsule declined and was similar to the contralateral side. However, the proportion of CD68-activated microglial cells remained higher than in the ispilateral external capsule. In addition, we measured microglial reaction in the external capsule after targeted ablation of pure population of layer II projection neurons. To this end, we performed in utero electroporation at E18, the timing when layer II neurons are generated; and induced neuronal death at P15 by DT injection. Similarly to previous observations, death of layer II neurons in somatosensory cortex triggered distant microglial activation doubling content of CD68-positive microglial cells in the external capsule (Supplementary Fig. S6). Together these data confirm that degeneration of axons due to the apoptotic death of cortical neurons induces long-lasting activation of microglial cells.

Discussion

Apoptotic neuronal death is a key feature of perinatal brain damage and neurodegenerative disorders. The results from our specific cortical neuronal ablation model with secondary consequences on white matter integrity challenge the viewpoint of primary vulnerability of white matter in preterm brain injury. It is increasingly recognized that moderate cell death without macroscopically detectable focal lesions could represent the initial step of a chronic pathological process leading to long-term alterations in neurodevelopment and altered cognitive functions in preterm infants (Kinney 2009; Dean et al. 2011; Ball et al. 2012). While advanced MRI techniques have been successfully used to detect massive apoptotic/necrotic cell death in the brain (van de Looij et al. 2011a); to date no evidence is available whether subtle, histologically verified apoptotic death could be detected by these noninvasive techniques. Here, we took advantage of our recently developed animal model (Petrenko et al. 2015) that allowed the precise spatiotemporal control of moderate apoptotic neuronal death in the rat cerebral cortex and demonstrate the ability of high-resolution MRI techniques to identify distinct phases of the acute apoptotic as well as postinjury, delayed processes involving the cerebral cortex and the underlying white matter. The MRI-based quantitative parameters of white and gray matter changes we describe here bring objectivity to the method and could be compared in different laboratories.

To the best of our knowledge, this is the first report showing the utility of in vivo ^{1}H-MRS imaging as biomarker of histologically verified moderate apoptotic cell death in the brain. ^{1}H-MRS imaging detected a significant decline of neuronal markers, NAA and NAAG specifically over the apoptotic cortical region. It is generally maintained that these metabolites reflect not just the number of neurons but also their metabolic status (Lei et al. 2009). In patients with perinatal hypoxic-ischemic encephalopathy, the decline in absolute concentration of NAA was sufficient to predict poor individual neurodevelopmental outcome (Boichot et al. 2006; Ancora et al. 2010). It was also shown that the concentration of NAAG also decreases early after hypoxic-ischemic injury in immature rat brain (van de Looij et al. 2011a). We extend these observations by showing that both metabolites could be a direct biomarker of early phases of apoptotic neuronal death.

Our data also show that ^{1}H-MRS imaging is able to detect reactive gliosis. The development of astroglial reaction was associated with an increase of myo-inositol concentration that is thought to be a glial-specific marker that could be monitored in many neurological diseases (Brand et al. 1993). Its concentration increases early after hypoxic-ischemic injury in animal model (van de Looij et al. 2011a) and in pediatric patients (Robertson et al. 2001; Ancora et al. 2010). Importantly, augmented concentration of this metabolite in the post-apoptotic cortex correlates with the persistence of the reactive astrogliosis hence it could be used for the post-apoptotic detection of the injured regions when other markers of acute injury are returned to normal values. Astrocytes are involved in the neurotransmitter recycling by participating in Glu–Gln cycle that can be assessed with noninvasive ^{1}H-MRS (Gruetter et al. 1998; Shen 2013). We observed a decline in Glu/Gln ratio

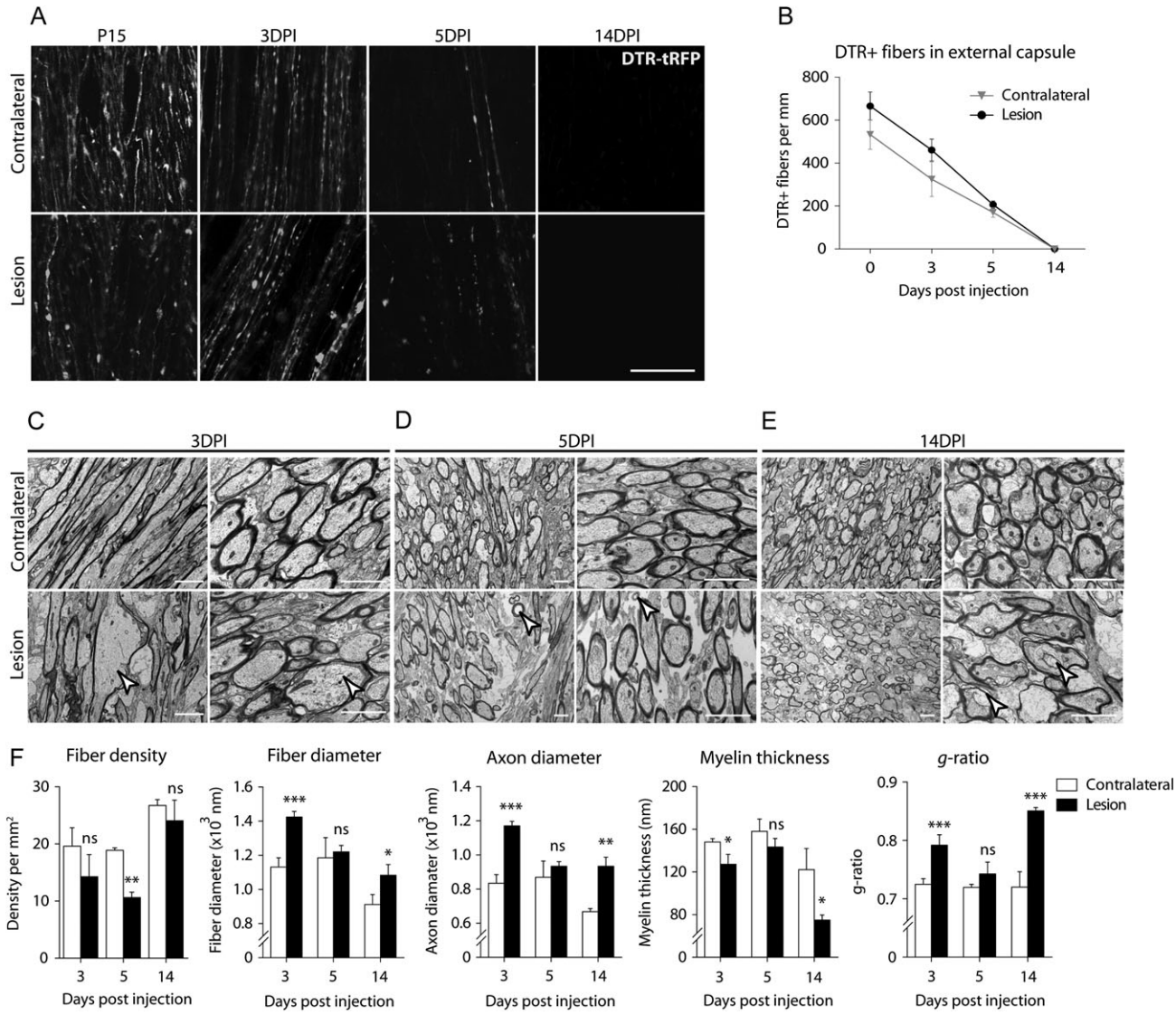

Figure 7. Delayed histopathological changes in the white matter occur after cortical neuronal ablation. (*A*) Confocal photos displaying loss of DTR-positive fibers labeled with tRFP and (*B*) corresponding graph representing decrease density of DTR-positive fibers per mm. Scale bar = 20 μm. (*C*–*E*) Electron micrographs illustrating ultrastructural changes in the external capsule in lesioned and contralateral hemispheres at indicated time points. White arrowheads indicate typical changes: Focal swelling of the axons with local disorganization of neurofilaments at 3 DPI (*C*); empty myelin sheath lacking axons located in swollen extracellular space at 5 DPI (*D*); intramyelinic swelling and splitting of myelin sheath at 14 DPI (*E*). Scale bars = 2 μm. (*F*) Histograms displaying morphometric data (mean fibers density, fiber diameter, axon diameter, myelin thickness, and *g*-ratio) of myelinated fibers in the ipsilateral and contralateral external capsules. Data expressed as a mean ± SEM, $^{*}P < 0.05$, $^{**}P < 0.01$, and $^{***}P < 0.001$ (unpaired 2-tailed *t*-test for $n = 3$).

coinciding with reactive astrogliosis starting from the end of the apoptotic period. Notably in the post-apoptotic period it was associated with higher glutamine concentration indicating accumulation of this metabolite in the tissue. Such a decline is thought to be a marker of a dysfunction of the Glu–Gln cycle (Tkac et al. 2001). Disruption of Gln–Glu cycle was previously described for neurological diseases associated with the reactive gliosis such as neurodegenerative diseases, Alexander disease and stroke (Robinson 2001; Seifert et al. 2006; Meisingset et al. 2010).

While the anatomical T_2W images failed to detect any macroscopical alterations in the apoptotic area, very similar to in vivo human imaging in preterm infants, high-field DTI allowed us to identify microstructural changes as early as 3 days after inducing cell death. We observed significantly increased water diffusivity in the injured area during the acute as well as during the late phase of apoptosis. Previous studies demonstrated that water diffusivity measures are correlated to microstructure integrity of the cortical tissue and enhanced diffusivity values reflect a reduced architectural state. For example, it was recently shown ex vivo on a fetal sheep model of mild cerebral ischemia without neuronal loss that the increased FA in the cortex was associated with the reduced complexity of basal dendrites of pyramidal neurons (Dean et al. 2013). Our results lend strong support to this notion by demonstrating an association between increased diffusivity values and the progressively reduced dendritic arbors of dying neurons. In addition, they provide proof of principle that DTI imaging is a sensible biomarker of a moderate, layer specific neuronal loss in the cerebral cortex. Interestingly, FA, reflecting the organization of the tissue, did not change during the

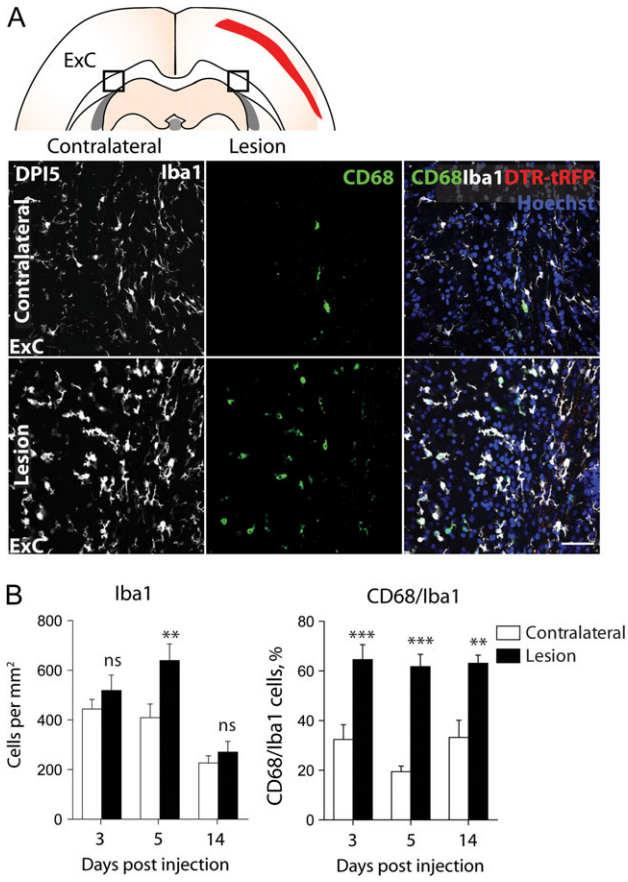

Figure 8. Activation of microglial cells in the white matter. (*A*) Representative confocal photos displaying the distribution of Iba1-positive microglial cells and their colocalization with CD68, a marker of activated microglia, in the lesioned and contralateral external capsules. Note single GFP-labeled axons in the external capsule at 14 DPI outgrowing from the survived electroporated confirming of both hemispheres successful electroporation. (*B*) Histograms representing number of Iba1-positive microglial cells and proportion of CD68-positive microglial cells in the external capsule of both hemispheres at indicated time points. Data expressed as a mean ± SEM, $^{**}P < 0.01$ and $^{***}P < 0.001$ (paired 2-tailed *t*-test, $n = 5$ animals per group). Scale bar = 50 μm.

apoptotic death process indicating a general increase of diffusivity in all direction. On the other hand, we observed significantly higher FA values during the post-apoptotic period revealing a disproportional increase of diffusivity: More enhanced in the axial direction and less in the radial direction. We discovered that these changes were correlated with a progressively increased dendritic arborization of surviving neurons mainly in the radial direction. These results demonstrate for the first time that DTI analysis is a valuable tool to assess not only subtle cell death-induced architectural loss in the cortical tissue but also the subsequent neuronal plasticity in the apoptotic neighborhood.

Since targeted cell death in our model not only involved layer IV neurons but also pyramidal cells in layer II/III with long distance projections, axonal degeneration in subcortical white matter was predictable. Indeed, DTI results revealed early microstructural changes correlated with the initial axonopathy and mild myelination deficit in the ipsilateral external capsule with an increased $D_{//}$ measured on DTI. It is assumed that changes in $D_{//}$ reflect axonal pathology (Alexander et al. 2007; Aung et al. 2013). Previous studies reported that severe axonal damage with the fragmentation of axons such as Wallerian degeneration or diffuse axonal injury are associated with the decline of $D_{//}$ in adult humans (Arfanakis et al. 2002; Song et al. 2003; Liu et al. 2013) as well as in rat model of traumatic brain injury (van de Looij et al. 2012). Here, we failed to find disrupted axons in the early apoptotic stage that together with the increase of mean axonal diameter could explain the observed increase of water diffusivity along the swollen axons. The acute primary degenerative process in axons, likely extended from dying cortical neurons, shares morphological features with early stages immune-mediated focal axonal damage in models of multiple sclerosis developing even prior the demyelination (Aboul-Enein et al. 2006; Nikic et al. 2011).

Five days after triggering cell death, an increase in water diffusivity in all directions was detectable by DTI that was simultaneous with a significant loss of myelinated fibers and an expansion of extracellular space even without detectable pathology of surviving axons or alteration of their myelin sheath. At this irreversible stage, primary damaged fibers have been eliminated. Our data suggest that the diffusivity values are rather affected by the density of myelinated fibers. Decline in FA is another important DTI derived parameter in the perinatal brain injuries and it was shown to be a reliable biomarker of adverse neurodevelopmental outcome (Huppi et al. 2001; Skranes et al. 2007; Counsell et al. 2008; Ment et al. 2009; Chau et al. 2013). In these studies, we demonstrated that the decreased FA in the ipsilateral external capsule reflects loss of myelinated fibers resulting from the targeted neuronal death in the cortex. These results are consistent with a previous study that showed a decrease in FA in the ipsilateral to the lesion external capsule associated with the reduced myelin without decreased axonal density after perinatal hypoxic-ischemic injury (Wang et al. 2009). Decline in white matter FA is an important predictor of adverse neurodevelopmental outcome in such patients (Skranes et al. 2007; Counsell et al. 2008; Ment et al. 2009; Ancora et al. 2013; Chau et al. 2013) and is reflecting hypomyelination of white matter tracts (Sakuma et al. 1991; Huppi et al. 2001; Inder et al. 2003; Wang et al. 2008).

An important observation of the current study is that delayed myelin abnormalities and hypomyelination of surviving fibers in the ipsilateral external capsule seem to follow the acute phase of axonal degeneration. These finding confirm previous neuropathological data indicating presence of hypomyelination in the white matter after hypoxic-ischemic and inflammation injuries (Billiards et al. 2008; Wang et al. 2008; Wang et al. 2009; Favrais et al. 2011). It has been proposed that alterations in myelin formation during the postinjury period are associated with high vulnerability of immature oligodendrocytes and their death either due to both hypoxic-ischemic or inflammatory injuries (Haynes et al. 2003; Volpe et al. 2011; Buser et al. 2012). In addition, myelin abnormalities with arrested maturation of oligodendrocyte progenitors into mature myelinating oligodendrocytes were also reported in preterm human brains (Billiards et al. 2008) and experimental models (Sizonenko et al. 2008; Favrais et al. 2011; Falahati et al. 2013; Back and Miller 2014). In the present model, we can exclude the primary death of immature oligodendrocytes. On the other hand, we showed an important activation of microglial cells in the external capsule starting from the timing of initial axonal degeneration. Recent studies indicate an important role of activated microglia in the development of perinatal white matter injuries (Kaur and Ling 2009; Volpe et al. 2011; Verney et al. 2012; Supramaniam et al. 2013; Baburamani et al. 2014; Mallard et al. 2014). Thus, an excessive activation of microglial cells on the axonal crossroads might disturb the normal developmental program (Verney et al. 2012). Our data

demonstrate that irreversible degeneration of axons due to the neuronal death in the cortex without primary hypoxia-ischemia or systemic inflammation is sufficient to induce microglial reaction in the ipsilateral external capsule. In turn, nitrites, reactive oxygen species, and pro-inflammatory cytokines produced locally by activated microglia may play important roles in development of secondary chronic demyelination as it has been shown in models of multiple sclerosis (Heppner et al. 2005; Bsibsi et al. 2014). The precise mechanism by which activation of microglial cells occur in our model as well as its role in observed hypomyelination remains to be determined.

In summary, the results of our study show that scattered apoptosis of cortical neurons may trigger, independently of hypoxia or overt lesion, MRI-defined delayed events in the developing cortex and in the white matter. These clinically relevant in vivo MRS and MRI techniques applied to this animal model and coupled with precise histological analyses provide invaluable observations for early recognition and monitoring injury events without macroscopic alterations in the immature brain.

Supplementary Material

Supplementary material are available at *Cerebral Cortex* online.

Funding

Swiss National Fund, Special Program University Medicine (SPUM) No 33CM30-124101/140334.

Notes

We wish to thank Cynthia Saadi and Elodie Husi for technical assistance. *Conflict of Interest*: None declared.

References

Aboul-Enein F, Weiser P, Hoftberger R, Lassmann H, Bradl M. 2006. Transient axonal injury in the absence of demyelination: a correlate of clinical disease in acute experimental autoimmune encephalomyelitis. Acta Neuropathol. 111:539–547.

Alexander AL, Lee JE, Lazar M, Field AS. 2007. Diffusion tensor imaging of the brain. Neurotherapeutics. 4:316–329.

Ancora G, Soffritti S, Lodi R, Tonon C, Grandi S, Locatelli C, Nardi L, Bisacchi N, Testa C, Tani G, et al. 2010. A combined a-EEG and MR spectroscopy study in term newborns with hypoxic-ischemic encephalopathy. Brain Dev. 32:835–842.

Ancora G, Testa C, Grandi S, Tonon C, Sbravati F, Savini S, Manners DN, Gramegna LL, Tani G, Malucelli E, et al. 2013. Prognostic value of brain proton MR spectroscopy and diffusion tensor imaging in newborns with hypoxic-ischemic encephalopathy treated by brain cooling. Neuroradiology. 55:1017–1025.

Andiman SE, Haynes RL, Trachtenberg FL, Billiards SS, Folkerth RD, Volpe JJ, Kinney HC. 2010. The cerebral cortex overlying periventricular leukomalacia: analysis of pyramidal neurons. Brain Pathol. 20:803–814.

Arfanakis K, Haughton VM, Carew JD, Rogers BP, Dempsey RJ, Meyerand ME. 2002. Diffusion tensor MR imaging in diffuse axonal injury. AJNR Am J Neuroradiol. 23:794–802.

Aung WY, Mar S, Benzinger TL. 2013. Diffusion tensor MRI as a biomarker in axonal and myelin damage. Imaging Med. 5:427–440.

Baburamani AA, Supramaniam VG, Hagberg H, Mallard C. 2014. Microglia toxicity in preterm brain injury. Reprod Toxicol. 48:106–112.

Back SA, Miller SP. 2014. Brain injury in premature neonates: a primary cerebral dysmaturation disorder? Ann Neurol. 75:469–486.

Ball G, Boardman JP, Rueckert D, Aljabar P, Arichi T, Merchant N, Gousias IS, Edwards AD, Counsell SJ. 2012. The effect of preterm birth on thalamic and cortical development. Cereb Cortex. 22:1016–1024.

Ball G, Srinivasan L, Aljabar P, Counsell SJ, Durighel G, Hajnal JV, Rutherford MA, Edwards AD. 2013. Development of cortical microstructure in the preterm human brain. Proc Natl Acad Sci U S A. 110:9541–9546.

Beck S, Wojdyla D, Say L, Betran AP, Merialdi M, Requejo JH, Rubens C, Menon R, Van Look PF.. 2010. The worldwide incidence of preterm birth: a systematic review of maternal mortality and morbidity. Bull World Health Organ. 88:31–38.

Billiards SS, Haynes RL, Folkerth RD, Borenstein NS, Trachtenberg FL, Rowitch DH, Ligon KL, Volpe JJ, Kinney HC. 2008. Myelin abnormalities without oligodendrocyte loss in periventricular leukomalacia. Brain Pathol. 18:153–163.

Boichot C, Walker PM, Durand C, Grimaldi M, Chapuis S, Gouyon JB, Brunotte F. 2006. Term neonate prognoses after perinatal asphyxia: contributions of MR imaging, MR spectroscopy, relaxation times, and apparent diffusion coefficients. Radiology. 239:839–848.

Brand A, Richter-Landsberg C, Leibfritz D.. 1993. Multinuclear NMR studies on the energy metabolism of glial and neuronal cells. Dev Neurosci. 15:289–298.

Bsibsi M, Peferoen LA, Holtman IR, Nacken PJ, Gerritsen WH, Witte ME, van Horssen J, Eggen BJ, van der Valk P, Amor S, et al. 2014. Demyelination during multiple sclerosis is associated with combined activation of microglia/macrophages by IFN-gamma and alpha B-crystallin. Acta Neuropathol. 128:215–229.

Buser JR, Maire J, Riddle A, Gong X, Nguyen T, Nelson K, Luo NL, Ren J, Struve J, Sherman LS, et al. 2012. Arrested preoligodendrocyte maturation contributes to myelination failure in premature infants. Ann Neurol. 71:93–109.

Chau V, Synnes A, Grunau RE, Poskitt KJ, Brant R, Miller SP. 2013. Abnormal brain maturation in preterm neonates associated with adverse developmental outcomes. Neurology. 81:2082–2089.

Counsell SJ, Edwards AD, Chew AT, Anjari M, Dyet LE, Srinivasan L, Boardman JP, Allsop JM, Hajnal JV, Rutherford MA, et al. 2008. Specific relations between neurodevelopmental abilities and white matter microstructure in children born preterm. Brain. 131:3201–3208.

Dean JM, McClendon E, Hansen K, Azimi-Zonooz A, Chen K, Riddle A, Gong X, Sharifnia E, Hagen M, Ahmad T, et al. 2013. Prenatal cerebral ischemia disrupts MRI-defined cortical microstructure through disturbances in neuronal arborization. Sci Transl Med. 5:168ra7.

Dean JM, van de Looij Y, Sizonenko SV, Lodygensky GA, Lazeyras F, Bolouri H, Kjellmer I, Huppi PS, Hagberg H, Mallard C. 2011. Delayed cortical impairment following lipopolysaccharide exposure in preterm fetal sheep. Ann Neurol. 70:846–856.

Dubois J, Benders M, Borradori-Tolsa C, Cachia A, Lazeyras F, Ha-Vinh Leuchter R, Sizonenko SV, Warfield SK, Mangin JF, Huppi PS. 2008. Primary cortical folding in the human newborn: an early marker of later functional development. Brain. 131:2028–2041.

Falahati S, Breu M, Waickman AT, Phillips AW, Arauz EJ, Snyder S, Porambo M, Goeral K, Comi AM, Wilson MA, et al. 2013. Ischemia-induced neuroinflammation is associated with disrupted development of oligodendrocyte progenitors in a model of periventricular leukomalacia. Dev Neurosci. 35:182–196.

Favrais G, van de Looij Y, Fleiss B, Ramanantsoa N, Bonnin P, Stoltenburg-Didinger G, Lacaud A, Saliba E, Dammann O, Gallego J, et al. 2011. Systemic inflammation disrupts the developmental program of white matter. Ann Neurol. 70: 550–565.

Folkerth RD. 2005. Neuropathologic substrate of cerebral palsy. J Child Neurol. 20:940–949.

Gruetter R, Seaquist ER, Kim S, Ugurbil K. 1998. Localized in vivo 13C-NMR of glutamate metabolism in the human brain: initial results at 4 tesla. Dev Neurosci. 20:380–388.

Gruetter R, Tkac I. 2000. Field mapping without reference scan using asymmetric echo-planar techniques. Magn Reson Med. 43:319–323.

Hasan KM, Parker DL, Alexander AL. 2001. Comparison of gradient encoding schemes for diffusion-tensor MRI. J Magn Reson Imaging. 13:769–780.

Haynes RL, Folkerth RD, Keefe RJ, Sung I, Swzeda LI, Rosenberg PA, Volpe JJ, Kinney HC. 2003. Nitrosative and oxidative injury to premyelinating oligodendrocytes in periventricular leukomalacia. J Neuropathol Exp Neurol. 62:441–450.

Heppner FL, Greter M, Marino D, Falsig J, Raivich G, Hovelmeyer N, Waisman A, Rulicke T, Prinz M, Priller J, et al. 2005. Experimental autoimmune encephalomyelitis repressed by microglial paralysis. Nat Med. 11:146–152.

Huppi PS, Murphy B, Maier SE, Zientara GP, Inder TE, Barnes PD, Kikinis R, Jolesz FA, Volpe JJ. 2001. Microstructural brain development after perinatal cerebral white matter injury assessed by diffusion tensor magnetic resonance imaging. Pediatrics. 107:455–460.

Inder TE, Warfield SK, Wang H, Huppi PS, Volpe JJ. 2005. Abnormal cerebral structure is present at term in premature infants. Pediatrics. 115:286–294.

Inder TE, Wells SJ, Mogridge NB, Spencer C, Volpe JJ. 2003. Defining the nature of the cerebral abnormalities in the premature infant: a qualitative magnetic resonance imaging study. J Pediatr. 143:171–179.

Johnson S, Marlow N. 2011. Preterm birth and childhood psychiatric disorders. Pediatr Res. 69:11R–18R.

Johnston MV, Trescher WH, Ishida A, Nakajima W. 2001. Neurobiology of hypoxic-ischemic injury in the developing brain. Pediatr Res. 49:735–741.

Kaur C, Ling EA. 2009. Periventricular white matter damage in the hypoxic neonatal brain: role of microglial cells. Prog Neurobiol. 87:264–280.

Kinney HC. 2009. The encephalopathy of prematurity: one pediatric neuropathologist's perspective. Semin Pediatr Neurol. 16:179–190.

Kinney HC, Haynes RL, Xu G, Andiman SE, Folkerth RD, Sleeper LA, Volpe JJ. 2012. Neuron deficit in the white matter and subplate in periventricular leukomalacia. Ann Neurol. 71: 397–406.

Lei H, Berthet C, Hirt L, Gruetter R. 2009. Evolution of the neurochemical profile after transient focal cerebral ischemia in the mouse brain. J Cereb Blood Flow Metab. 29:811–819.

Liu M, Gross DW, Wheatley BM, Concha L, Beaulieu C. 2013. The acute phase of Wallerian degeneration: longitudinal diffusion tensor imaging of the fornix following temporal lobe surgery. Neuroimage. 74:128–139.

Mallard C, Davidson JO, Tan S, Green CR, Bennet L, Robertson NJ, Gunn AJ. 2014. Astrocytes and microglia in acute cerebral injury underlying cerebral palsy associated with preterm birth. Pediatr Res. 75:234–240.

Meisingset TW, Risa O, Brenner M, Messing A, Sonnewald U. 2010. Alteration of glial-neuronal metabolic interactions in a mouse model of Alexander disease. Glia. 58:1228–1234.

Ment LR, Hirtz D, Huppi PS. 2009. Imaging biomarkers of outcome in the developing preterm brain. Lancet Neurol. 8: 1042–1055.

Mlynarik V, Gambarota G, Frenkel H, Gruetter R. 2006. Localized short-echo-time proton MR spectroscopy with full signal-intensity acquisition. Magn Reson Med. 56:965–970.

Nikic I, Merkler D, Sorbara C, Brinkoetter M, Kreutzfeldt M, Bareyre FM, Bruck W, Bishop D, Misgeld T, Kerschensteiner M. 2011. A reversible form of axon damage in experimental autoimmune encephalomyelitis and multiple sclerosis. Nat Med. 17:495–499.

Northington FJ, Chavez-Valdez R, Martin LJ. 2011. Neuronal cell death in neonatal hypoxia-ischemia. Ann Neurol. 69: 743–758.

Petrenko V, Mihhailova J, Salmon P, Kiss JZ. 2015. Apoptotic neurons induce proliferative responses of progenitor cells in the postnatal neocortex. Exp Neurol. 273:126–137.

Pierson CR, Folkerth RD, Billiards SS, Trachtenberg FL, Drinkwater ME, Volpe JJ, Kinney HC. 2007. Gray matter injury associated with periventricular leukomalacia in the premature infant. Acta Neuropathol. 114:619–631.

Provencher SW. 1993. Estimation of metabolite concentrations from localized in vivo proton NMR spectra. Magn Reson Med. 30:672–679.

Robertson NJ, Lewis RH, Cowan FM, Allsop JM, Counsell SJ, Edwards AD, Cox IJ. 2001. Early increases in brain myo-inositol measured by proton magnetic resonance spectroscopy in term infants with neonatal encephalopathy. Pediatr Res. 50:692–700.

Robinson SR. 2001. Changes in the cellular distribution of glutamine synthetase in Alzheimer's disease. J Neurosci Res. 66:972–980.

Saito T, Nakatsuji N. 2001. Efficient gene transfer into the embryonic mouse brain using in vivo electroporation. Dev Biol. 240:237–246.

Sakuma H, Nomura Y, Takeda K, Tagami T, Nakagawa T, Tamagawa Y, Ishii Y, Tsukamoto T. 1991. Adult and neonatal human brain: diffusional anisotropy and myelination with diffusion-weighted MR imaging. Radiology. 180:229–233.

Seifert G, Schilling K, Steinhauser C. 2006. Astrocyte dysfunction in neurological disorders: a molecular perspective. Nat Rev Neurosci. 7:194–206.

Shen J. 2013. Modeling the glutamate-glutamine neurotransmitter cycle. Front Neuroenergetics. 5:1.

Sizonenko SV, Camm EJ, Dayer A, Kiss JZ. 2008. Glial responses to neonatal hypoxic-ischemic injury in the rat cerebral cortex. Int J Dev Neurosci. 26:37–45.

Skranes J, Vangberg TR, Kulseng S, Indredavik MS, Evensen KA, Martinussen M, Dale AM, Haraldseth O, Brubakk AM. 2007. Clinical findings and white matter abnormalities seen on diffusion tensor imaging in adolescents with very low birth weight. Brain. 130:654–666.

Song SK, Sun SW, Ju WK, Lin SJ, Cross AH, Neufeld AH. 2003. Diffusion tensor imaging detects and differentiates axon and myelin degeneration in mouse optic nerve after retinal ischemia. Neuroimage. 20:1714–1722.

Supramaniam V, Vontell R, Srinivasan L, Wyatt-Ashmead J, Hagberg H, Rutherford M. 2013. Microglia activation in the extremely preterm human brain. Pediatr Res. 73:301–309.

Tkac I, Keene CD, Pfeuffer J, Low WC, Gruetter R. 2001. Metabolic changes in quinolinic acid-lesioned rat striatum detected non-invasively by in vivo (1)H NMR spectroscopy. J Neurosci Res. 66:891–898.

Tkac I, Rao R, Georgieff MK, Gruetter R. 2003. Developmental and regional changes in the neurochemical profile of the rat brain determined by in vivo 1 H NMR spectroscopy. Magn Reson Med. 50:24–32.

van de Looij Y, Chatagner A, Huppi PS, Gruetter R, Sizonenko SV. 2011a. Longitudinal MR assessment of hypoxic ischemic injury in the immature rat brain. Magn Reson Med. 65:305–312.

van de Looij Y, Kunz N, Huppi P, Gruetter R, Sizonenko S. 2011b. Diffusion tensor echo planar imaging using surface coil transceiver with a semiadiabatic RF pulse sequence at 14.1T. Magn Reson Med. 65:732–737.

van de Looij Y, Mauconduit F, Beaumont M, Valable S, Farion R, Francony G, Payen JF, Lahrech H. 2012. Diffusion tensor imaging of diffuse axonal injury in a rat brain trauma model. NMR Biomed. 25:93–103.

Verney C, Pogledic I, Biran V, Adle-Biassette H, Fallet-Bianco C, Gressens P. 2012. Microglial reaction in axonal crossroads is a hallmark of noncystic periventricular white matter injury in very preterm infants. J Neuropathol Exp Neurol. 71:251–264.

Vinall J, Grunau RE, Brant R, Chau V, Poskitt KJ, Synnes AR, Miller SP. 2013. Slower postnatal growth is associated with delayed cerebral cortical maturation in preterm newborns. Sci Transl Med. 5:168ra8.

Volpe JJ. 2009. Brain injury in premature infants: a complex amalgam of destructive and developmental disturbances. Lancet Neurol. 8:110–124.

Volpe JJ, Kinney HC, Jensen FE, Rosenberg PA. 2011. The developing oligodendrocyte: key cellular target in brain injury in the premature infant. Int J Dev Neurosci. 29:423–440.

Wang S, Wu EX, Cai K, Lau HF, Cheung PT, Khong PL. 2009. Mild hypoxic-ischemic injury in the neonatal rat brain: longitudinal evaluation of white matter using diffusion tensor MR imaging. AJNR Am J Neuroradiol. 30:1907–1913.

Wang S, Wu EX, Tam CN, Lau HF, Cheung PT, Khong PL. 2008. Characterization of white matter injury in a hypoxic-ischemic neonatal rat model by diffusion tensor MRI. Stroke. 39:2348–2353.

Wasterlain CG, Niquet J, Thompson KW, Baldwin R, Liu H, Sankar R, Mazarati AM, Naylor D, Katsumori H, Suchomelova L, et al. 2002. Seizure-induced neuronal death in the immature brain. Prog Brain Res. 135:335–353.

Zhu C, Wang X, Xu F, Bahr BA, Shibata M, Uchiyama Y, Hagberg H, Blomgren K. 2005. The influence of age on apoptotic and other mechanisms of cell death after cerebral hypoxia-ischemia. Cell Death Differ. 12:162–176.